

EPOFusion: Exposure-aware Progressive Optimization Method for Infrared and Visible Image Fusion

Zhiwei Wang, Yayu Zheng, Defeng He*, Li Zhao, Xiaoqin Zhang, *Senior Member, IEEE*,
Yuxing Li, Edmund Y. Lam, *Fellow, IEEE*

Abstract—Overexposure frequently occurs in practical scenarios, causing the loss of critical visual information. However, existing infrared and visible fusion methods still exhibit unsatisfactory performance in highly bright regions. To address this, we propose EPOFusion, an exposure-aware fusion model. Specifically, a guidance module is introduced to facilitate the encoder in extracting fine-grained infrared features from overexposed regions. Meanwhile, an iterative decoder incorporating a multi-scale context fusion module is designed to progressively enhance the fused image, ensuring consistent details and superior visual quality. Finally, an adaptive loss function dynamically constrains the fusion process, enabling an effective balance between the modalities under varying exposure conditions. To achieve better exposure awareness, we construct the first infrared-visible overexposure (IVOE) dataset with high quality infrared guided annotations for overexposed regions. Extensive experiments show that EPOFusion outperforms existing methods. It maintains infrared cues in overexposed regions while achieving visually faithful fusion in non-overexposed areas, thereby enhancing both visual fidelity and downstream task performance. Code, fusion results and IVOE dataset will be made available at <https://github.com/warren-wzw/EPOFusion.git>.

Index Terms—Image fusion, overexposure, infrared image, visible image, iterative optimization, adaptive loss function.

I. INTRODUCTION

INFRARED and visible Image fusion plays a key role in applications such as intelligent surveillance [1], [2] and autonomous driving [3], [4]. In scenarios with normal illumination, visible images provide rich textural details that complement the thermal targets in infrared images. However, realistic environments frequently present severe overexposure challenges, such as strong daylight or intense glare during night driving. Overexposure introduces specific obstacles that render standard fusion paradigms ineffective. Specifically, visible sensors suffer from pixel saturation, where high-intensity regions contain no valid gradients or texture [5].

This work was supported partly by the National Natural Science Foundation of China under Grant No. U24A20270 and U24A20242, and National Key R&D Program of China under Grant No.2024YFC3306901.

Zhiwei Wang, Yayu Zheng, Defeng He and Xiaoqin Zhang are with the College of Information Engineering, Zhejiang University of Technology, Hangzhou 310023, China (e-mail: wzw@zjut.edu.cn, yayuzheng@zjut.edu.cn, hdfzj@zjut.edu.cn, xqzhang@zjut.edu.cn).

Li Zhao is with the College of Information Science and Technology, Zhejiang Shuren University, Hangzhou, 310015, China (e-mail: zhaoli@zjsru.edu.cn).

Yuxing Li and Edmund Y. Lam are with the Department of Electrical and Electronic Engineering, The University of Hong Kong, Hong Kong, China (e-mail: yuxingli@hku.hk, elam@eee.hku.hk).

Zhiwei Wang is also a visiting Ph.D. student at the University of Hong Kong, Hong Kong, China (e-mail: wangzw@eee.hku.hk).

*Corresponding authors: Defeng He.

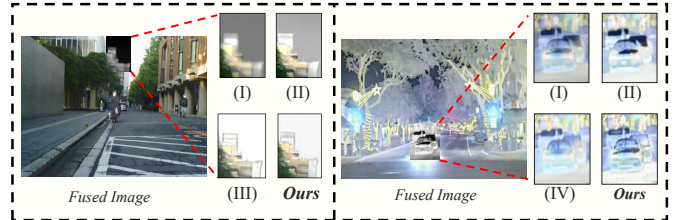


Fig. 1: (I) Generative prior-based framework. (II) Downstream task-guided approach. (III–IV) Handcrafted loss-guided strategies: (III) texture-dominated optimization and (IV) intensity-dominated optimization.

Existing approaches often lack robustness when handling high-exposure regions. Certain methods tend to be dominated by saturated visible intensity, resulting in the complete loss of thermal details. Conversely, some methods designed to maximize the preservation of infrared information often inadvertently amplify sensor noise, thus degrading image clarity. Therefore, effective fusion of visible and infrared images while preserving critical infrared information under extreme exposure conditions remains a significant challenge.

In general, existing infrared and visible image fusion methods can be categorized into three groups based on the source of fusion objectives: generative prior-based [6], [7], downstream task-driven methods [4], [8] and handcrafted loss-guided [5], [9]. Generative prior-based methods are typically represented by Generative Adversarial Networks (GAN) [10] based approaches, which use adversarial training between a generator and a discriminator [6], [7]. This adversarial mechanism enables the model to implicitly learn the probability distribution of the source images, generating fused results with natural visual characteristics. To better exploit semantic information, task-driven methods jointly optimize fusion and high-level vision tasks, enabling semantic features to be effectively incorporated into the fusion process [4], [8], [11]. Handcrafted loss-guided methods constrain the network optimization process via carefully designed loss functions, thereby achieving an overall fusion of infrared and visible information. Their main advantage lies in their simplicity and computational efficiency [12], [13].

Existing approaches struggle to effectively handle high-exposure regions. As shown in Fig. 1, generative prior-based approaches often introduce background noise and global degradation, as their generators prioritize global fidelity over semantic constraints. Conversely, although task-driven methods preserve salient structures, they often fail to distinguish informative features, and thus introduce redundant infrared information, thereby degrading visual quality. Similarly, hand-

crafted loss-based methods fail to reveal details in high-exposure regions, as fixed loss functions cannot effectively capture the semantic complementarity between modalities. Consequently, achieving robust fusion under extreme lighting remains a significant challenge.

To address this, we propose EPOFusion, a fusion framework that utilizes iterative strategies to achieve progressive optimization. It uses a guidance module to steer the model attention toward infrared information in overexposed regions, thereby markedly recovering thermal details in these challenging areas. Inspired by the stepwise optimization in DDPM [14], an iterative fusion module is designed based on the denoising diffusion mechanism, enabling features to progressively reinforce critical information over multiple iterations. Furthermore, we constructed an adaptive fusion loss to dynamically guide the model in optimizing the overall fusion results, effectively preserving infrared details in high-exposure regions. Considering that existing public datasets contain few overexposed samples and lack corresponding annotations, we constructed a synthetic overexposure dataset, termed IVOE. Furthermore, we utilized the Segment Anything Model (SAM) [15] to assist in annotation, and selected image pairs from existing datasets for real-world evaluation. As shown in Fig. 1, the fusion results of our method clearly preserve the structure of the roof and maintain the intensity of the color, the sky appearing to be free of infrared noise. In addition, in night scenes, vehicle in overexposed areas remain clearly visible. The main contributions are summarized as follows:

- We propose EPOFusion, a region-guided, exposure-aware iterative framework that excels at preserving infrared details in overexposed regions.
- We designed a multi-scale context fusion module and an adaptive dynamic loss function that work together to guide the model toward detailed targets and enhance its robustness under extreme lighting conditions.
- We constructed the IVOE dataset with precise annotations of the details in the overexposed regions. Additionally, we also curated a test set of real-world overexposed pairs.
- Extensive experiments show that our model outperforms existing methods, producing clearer details in high-exposure regions and significantly enhancing the accuracy of downstream segmentation and detection tasks.

The remainder of this paper is organized as follows: Section II overviews the related work. Section III analyzes fusion challenges under overexposure and presents EPOFusion and the IVOE dataset. Section IV shows the experimental results and analysis, demonstrating the advantages of our method. Section V concludes the paper.

II. RELATED WORKS

A. Generative prior-based Image Fusion

Generative prior-based image fusion methods leverage the powerful distribution modeling capabilities of deep generative models to reconstruct high-quality fused images. Existing methods in this category are broadly categorized into GAN-based [6], [16], [17] and Denoising Diffusion Probabilistic Model (DDPM)-based [18]–[20]. Generative adversarial

framework have been widely adopted for image fusion due to their strong capability to generate high-quality and realistic images [10]. FusionGAN [6] pioneered the approach by formulating fusion as a generator–adversarial discriminator problem. Subsequent works like GANMcC [17] enhanced visual fidelity by employing multi-class estimation and incorporating fidelity losses [16] to optimize fusion outcomes. Unlike GAN, which suffers from training instability and mode collapse, DDPM [14] achieves stable target distribution convergence through a multi-step iterative process. Dif-Fusion [18] first introduced diffusion model, generating high-color-fidelity, three-channel fused images by constructing the multi-channel input distribution in a latent space. DDFM [19] regards fusion as a conditional generation task, decomposing it into unconditional generation and likelihood rectification based on a hierarchical Bayesian model to achieve high-quality fusion without fine-tuning. Although these methods can retain infrared and visible information to the greatest extent, they tend to introduce excessive infrared information when handling overexposed scenarios.

B. Handcrafted loss-guided Image Fusion

Handcrafted loss-guided image fusion methods design customized loss functions to guide the model in feature extraction, feature fusion, and pixel-wise reconstruction of the fused image, thereby ensuring high-quality fusion results [12], [13], [21]. SDNet [5] introduces a gradient loss with adaptive decision blocks in pixels, an intensity loss with task-adaptive weighting, and a loss in consistency of decomposition for joint optimization, making it effective and general in diverse fusion tasks. In addition, many existing methods commonly adopt texture loss to preserve structural and detail information [9], [22], along with intensity loss to maintain global brightness and contrast, jointly providing complementary constraints that balance detail preservation and visual fidelity in the fused image. Xie et al. [23] designed a specific prior module to generate overexposure masks, aiming to retain infrared features in high-exposure regions. Although this method is efficient and widely adopted, their performance critically depends on the design and weighting of the loss functions. This reliance makes it difficult to effectively preserve infrared information in challenging scenarios, such as those with severe overexposure.

C. Down-stream task-guided Image Fusion

Image fusion is often used as a preprocessing step for downstream vision tasks. Jointly optimizing image fusion with these tasks has become a growing trend [4], [8], [24]. TarDal [8] cascades image fusion with object detection, leveraging the loss of detection to guide the fusion model to preserve more relevant semantic information for detection. SegMif [4] employs a hierarchical interactive attention mechanism within a unified framework to enable bidirectional feature communication between fusion and segmentation tasks, combined with adaptive dynamic weights and interactive training, resulting in fused images that are both visually appealing and more conducive to semantic segmentation. TDFusion [25] proposes a task-driven learnable fusion loss that is optimized through meta-learning, allowing the fused images to effectively minimize

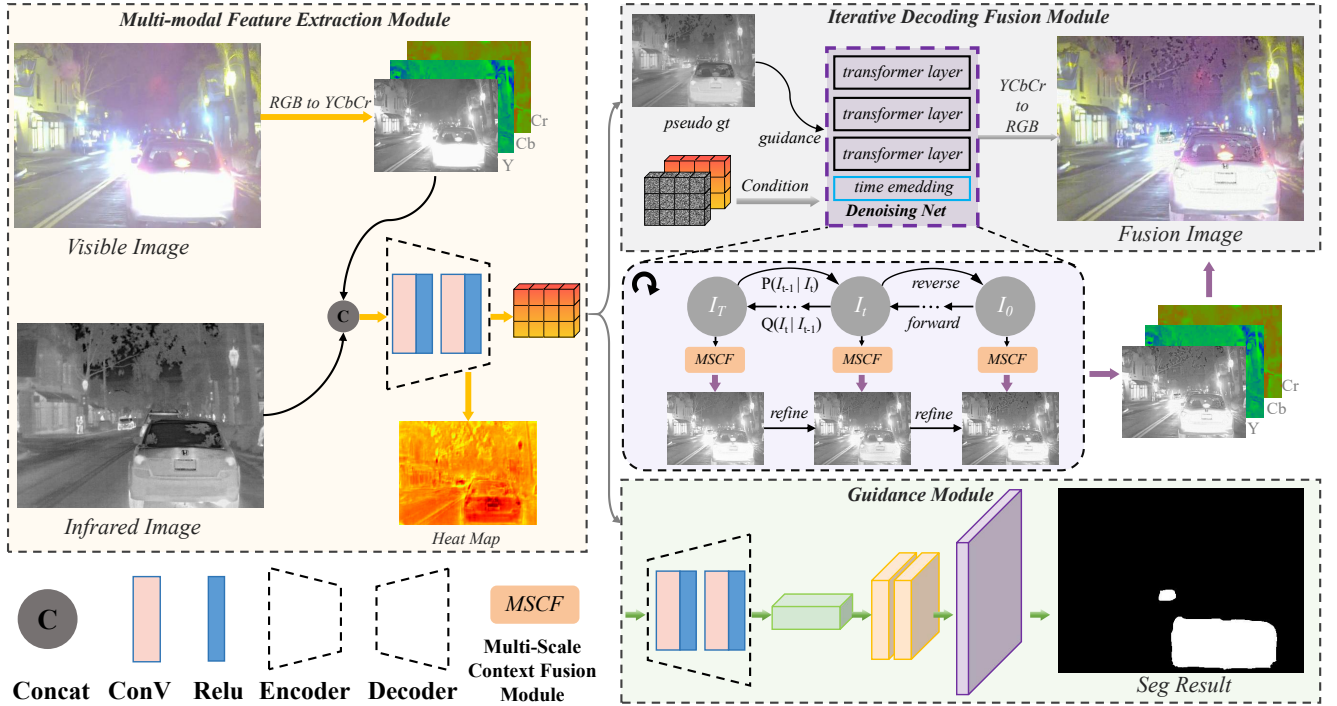


Fig. 2: The overall framework of EPOFusion, showing its main components and processing flow.

the loss of downstream tasks. In extreme lighting conditions, this method usually fails to accurately localize overexposed infrared regions based on semantic guidance, resulting in a loss of specific infrared details.

D. Infrared and visible image dataset

Numerous datasets have been established to facilitate research in infrared and visible image fusion. Widely used benchmarks such as MFNet [26], LLVIP [2], MSRS [27] and M³FD [8] provide abundant aligned image pairs with semantic or detection annotations, covering typical daytime and nighttime scenarios. Xie et al. [23] introduced a dataset focused on overexposure. They cropped collected images into 120×120 patches to construct the training set and selected 40 pairs for testing. Despite these advancements, public datasets remain scarce in overexposed samples and lack precise pixel-level annotations to guide the fusion process in these regions.

III. METHODOLOGY

In this section, we first analyze the problem of detail loss in RGBT image fusion under overexposed conditions. The following details the proposed EPOFusion framework, along with the construction of the IVOE dataset.

A. Problem Formulation

Consider a visible image I_{vi} and infrared image I_{ir} . The fusion process can be formulated as $I_f = \mathcal{F}(I_{vi}, I_{ir})$, where I_f denotes fused image. Ideally, I_f should retain complementary information from both modalities, preserving the structural and textural details of I_{vi} while incorporating prominent infrared features from I_{ir} . Furthermore, both I_{vi} and I_{ir} are expected

to be able to reconstruct from I_f , which can be formally expressed as follows:

$$I_{vi} = D_{vi}(I_f), I_{ir} = D_{ir}(I_f), \quad (1)$$

where D_{vi} and D_{ir} represent modality-specific decoders.

Handcrafted loss-guided frameworks typically employ intensity loss \mathcal{L}_{int} and texture losses \mathcal{L}_{tex} to guide the fusion process. However, they encounter a critical optimization conflict in overexposed areas. When \mathcal{L}_{int} dominates, the fused result tends to converge towards the visible image, retaining the saturated intensity in overexposed regions. In contrast, when \mathcal{L}_{tex} prevails, the fused image inherits the infrared texture but sacrifices crucial thermal intensity information. This dilemma is formulated as follows:

$$I_f \leftarrow \mathcal{L}_{total} = \lambda_{int} \mathcal{L}_{int} + \lambda_{tex} \mathcal{L}_{tex},$$

$$\rho_{int} = \frac{\|\lambda_{int} \nabla_{\theta} \mathcal{L}_{int}\|_2}{\|\nabla_{\theta} \mathcal{L}_{total}\|_2}, \quad \rho_{tex} = \frac{\|\lambda_{tex} \nabla_{\theta} \mathcal{L}_{tex}\|_2}{\|\nabla_{\theta} \mathcal{L}_{total}\|_2},$$

$$\Rightarrow \begin{cases} I_f^{OE} \approx I_{vi}^{OE}, & \rho_{int} > \rho_{tex}, \\ \|\Delta I_f^{OE} - \Delta I_{vi}^{OE}\| < \tau, I_f^{OE} \approx I_{ir}^{OE}, & \rho_{tex} > \rho_{int}, \end{cases} \quad (2)$$

where $\lambda_{int, tex}$ are the weights, $\|\cdot\|_2$ denotes the ℓ_2 norm, ∇_{θ} represents the gradient with respect to the network parameters, OE refers to the overexposed area, Δ is the Sobel operator, and τ is a small threshold.

Downstream task-driven fusion methods that prioritize texture are prone to conflicts in overexposed scenes. Specifically, the smooth, featureless regions of the visible image are juxtaposed with the low-signal infrared counterparts, where sensor noise predominates. Similarly, GAN-based fusion models struggle to discriminate between informative content and spurious artifacts, often retaining all signals indiscriminately.

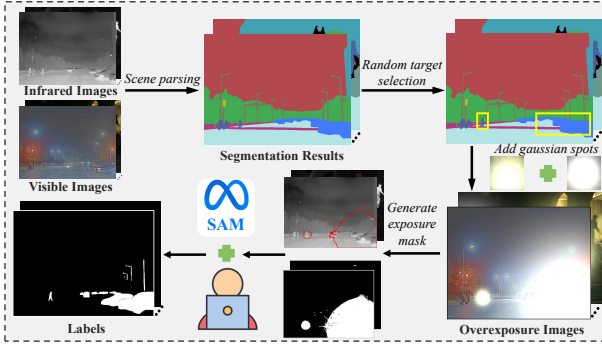


Fig. 3: An overview of the infrared-visible overexposure (IVOE) dataset construction pipeline.

Due to these shortcomings, the model fails to distinguish meaningful texture from noise, the model misinterprets the noise as a salient feature, and erroneously introduces it into the final image.

The goal of this paper is twofold: (i) to preserve salient infrared information in overexposed regions while suppressing noise and artifacts in non-salient areas; and (ii) to improve the accuracy of downstream tasks, such as segmentation and object detection, particularly in overexposed scenes.

B. Exposure Guided Fusion Framework

Overexposure often leads to the loss of critical infrared details. To address this issue, we propose an exposure aware fusion framework, as illustrated in Fig. 2. The core idea of our framework is to leverage explicit regional guidance with an adaptive fusion loss to accurately recover missing image details. Specifically, the framework consists of three key components: a multimodal feature extraction module, an iterative decoding fusion module, and a guidance module.

For each pair of visible I_{vi} and infrared I_{ir} images, we first convert the visible image from RGB to the YCbCr color space, with only the luminance (Y) channel employed as input. To efficiently extract complementary features, we adopt an early fusion strategy: the infrared image and the Y channel of the visible image are concatenated and fed into the encoder of ConvNeXt [28], which serves as the feature extractor. After passing through the multimodal feature extraction module, we obtain the fused feature \mathcal{F}_{fusion} . Then \mathcal{F}_{fusion} are processed in parallel by the iterative decoding fusion module and the guidance module. Through the decoder, we obtain the Y channel of the fused image. Finally, we combine this fused Y channel with the original Cb and Cr channels of the visible image and perform an inverse color-space transformation to reconstruct the final fused image.

The guidance module is designed to enhance the preservation of infrared details in overexposed regions by predicting an infrared mask for these areas. This mechanism explicitly directs the network to focus on objects within the overexposed regions. As illustrated in Fig. 2, the encoder heatmaps and fused results demonstrate that, with the assistance of the guidance network, the encoder of EPOFusion can accurately focus on details in overexposed areas, effectively preserve fine structures, and achieve robust performance under overexposure conditions.

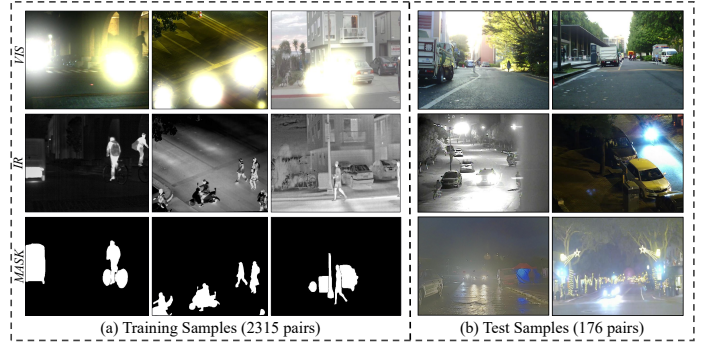


Fig. 4: Examples from the IVOE dataset. The training set is synthetically generated with accurate annotations, and the test set is collected from multiple public datasets.

C. Iterative Decoding Fusion Module

Traditional fusion decoders generally adopt a direct strategy that transforms the fused feature into the image space in a single step. Nevertheless, in challenging scenarios such as high-brightness regions, this one-shot approach often fails to fully exploit the fused feature, leading to incomplete multi-modal information integration. To overcome this limitation, we design an iterative decoding strategy that progressively reconstructs the fused image, thereby reducing one-shot bias and enhancing cross-modal information preservation.

1) *Iterative Refinement Mechanism*: Diffusion models recover a target distribution from noise via progressive generation [14]. We leverage this to model fusion as a step-wise iterative optimization of feature representations. Unlike methods requiring perfect ground truth, our framework relies only on representative samples to guide the reverse trajectory towards the target distribution. We treat this process as feature purification, where the model corrects latent inconsistencies and highlights salient structures through multi-step inference, which are finally decoded by the Multi-Scale Context Fusion (MSCF) module. To further improve the efficiency of the model, we use the sampling paradigm of denoising diffusion implicit models (DDIM) [29].

In the training process, we construct a simple pseudo ground truth $I_{pseudo} = 0.5I_{vi} + 0.5I_{ir}$ to serve as an effective distribution anchor. This constraint guides global convergence and supervises overexposed regions in the fusion result. Then I_{pseudo} is downsampled to form the feature $F_{gt} = (I_{pseudo})_{\downarrow}$, where $(\cdot)_{\downarrow}$ denotes downsampling process. Gaussian noise is added to F_{gt} to produce the noised target feature \mathcal{F}_{noised} . The fusion feature \mathcal{F}_{fusion} extracted from the multimodal input, is then concatenated with \mathcal{F}_{noised} and sent as a conditional input to the denoising network \mathcal{D}_{θ} . The denoised features $F_{denoised}$ are then decoded using the MSCF module to reconstruct the final fused image. The process can be described as follows:

$$\begin{aligned} F_{noised} &= \alpha_t F_{gt} + \beta_t \epsilon, \quad \epsilon \sim \mathcal{N}(0, 1), \\ F_{cond} &= F_{fusion} \oplus F_{noised}, \\ I_f &= MSCF(\mathcal{D}_{\theta}(F_{cond}, t)), \end{aligned} \quad (3)$$

where \oplus denotes concatenation, α_t and β_t are the coefficients controlling noise addition.

During the sampling process, we first draw an initial noise map $mask_t \sim \mathcal{N}(0, 1)$. The model then progressively refines

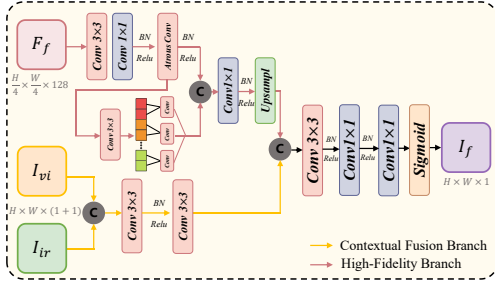


Fig. 5: The architecture of the Multi-Scale Context Fusion Module (MSCF).

this representation from $t = T - 1$ to $t = 0$. At each step, the current noise is combined with the fusion feature F_{fusion} and passed through the denoising network \mathcal{D}_θ to produce intermediate features $F_{denoise}$. These features are further decoded by the MSCF module to reconstruct the fused result. The latent noise is then estimated from the prediction result and used to update the noise map for the next step. Through this iterative refinement, the process eventually produces the final fused image I_f , which is expressed at each time step t as:

$$\begin{aligned} (\alpha_t, \beta_t, \alpha_{t-1}, \beta_{t-1}) &= \text{Cal}(t_{now}, t_{next}), \\ F_{denoise} &= \mathcal{D}_\theta(\text{mask}_t \oplus F_{fusion}, t_{now}), \\ \text{pred}_{noise} &= \frac{\text{mask}_t - \beta_t \cdot (I_f)_\downarrow}{\alpha_t}, \\ \text{mask}_t &= \alpha_{t-1} \cdot \text{pred}_{noise} + \beta_{t-1} \cdot (I_f)_\downarrow, \end{aligned} \quad (4)$$

where $\text{Cal}(\cdot)$ calculates the sampling coefficients for the current and next steps.

2) *Multi-Scale Context Fusion Module*: To effectively leverage the refined features from the iterative optimizer and enhance multi-scale, cross-modal feature interactions, we introduce the MSCF module. The MSCF is composed of two specialized pathways: a Contextual Fusion Branch (CFB) and a High-Fidelity Branch (HFB), designed to reconstruct high-quality fused images.

The CFB, as illustrated in Fig. 5, is designed to extract multi-scale contextual information from the denoised features $F_{denoise}$. To reduce computational redundancy, the input is first processed by a sequential convolutions. Subsequently, to capture both long-range dependencies and local details, we employ a dual-branch architecture. The first branch utilizes dilated convolutions to expand the receptive field, thereby gathering global contextual information. The second branch employs a cascade of standard and grouped convolutions to focus on fine-grained local features. Finally, the features from both branches are concatenated and fused via a 1×1 convolution to generate the high-level context representation F_{CFB} . This process is formulated as:

$$\begin{aligned} F_{global} &= \sigma_R(\text{BN}(\text{Conv}_{Atrous}(\text{Conv}(F_f))))), \\ F_s &= \text{Conv}_s((\hat{F}_f)_s), \quad s = 1, 2, \dots, G, \\ F_{fused} &= \text{Conv}_{1 \times 1}(F_{global} \oplus (F_1 \oplus F_2 \cdots \oplus F_G)), \\ F_{CFB} &= \sigma_R(\text{BN}(F_{fused})), \end{aligned} \quad (5)$$

where G denotes the total number of groups, $\text{BN}(\cdot)$ represents Batch Normalization, $\text{Conv}_{Atrous}(\cdot)$ indicates the atrous con-

volution, $\text{Conv}_{1 \times 1}(\cdot)$ refers to the point-wise convolution, and $\sigma_R(\cdot)$ is the relu activation function.

The HFB is designed to preserve fine-grained details from the source images. It begins by concatenating the visible image I_{vi} and the infrared image I_{ir} to create a dual-channel input. This is then processed by two consecutive convolution layers that extract essential low-level features, such as edges and textures, producing a detailed feature map F_{HFB} . This operation is formulated as:

$$F_{HFB} = \sigma_R(\text{BN}(\text{Conv}(\text{Conv}(I_{vi} \oplus I_{ir}))). \quad (6)$$

Finally, the features from both branches are fused. The high-level context from F_{CFB} and the detailed information from F_{HFB} are concatenated and passed through a refinement block Φ . This allows the network to intelligently balance and select complementary information from both sources. A final Sigmoid activation function is applied to generate the single-channel fused image I_f . The process can be expressed as:

$$I_f = \sigma_S(\Phi(F_{CFB} \oplus F_{HFB})), \quad (7)$$

where $\Phi(\cdot)$ denotes convolutional and non-linear operation, and $\sigma_S(\cdot)$ means sigmoid function.

D. Infrared-Visible Over-Exposure Dataset

Existing public datasets have limited overexposed samples and lack annotations that guide the model to focus on infrared features in overexposed areas, which poses a challenge for exposure-aware fusion. To address this, we constructed the IVOE dataset with controlled exposure levels, simulating various lighting conditions and providing pixel-level annotations. This allows the model to recognize important details while preserving key information in exposed regions. Additionally, we collected 176 real overexposure infrared-visible image pairs from public datasets to further validate the performance of our model.

The pipeline for constructing the IVOE dataset is illustrated in Fig. 3. We first collect a comprehensive set of infrared-visible pairs from public datasets, including MFNet [26], LLVIP [2], M³FD [8] and VIFB [30]. Then, we employ the pretrained DiFusionSeg model [24] to perform scene parsing, yielding pixel-level segmentation masks. Based on the masks, we identify all object instances belonging to key foreground categories (e.g., person, car, bus, truck, motor). Then, we randomly sample a subset and synthetically generate overexposure by overlaying Gaussian light spots with varying intensities from 1.0 to 1.6, and color tones (white or yellowish). The light distribution is modeled using a spatial Gaussian kernel centered on each selected object, enabling realistic exposure blooming. In this manner, both localized and global overexposure effects are synthesized while preserving scene structure. Subsequently, we detect the overexposed regions via thresholding, extract their contours, and project these contours onto the corresponding infrared images as visual references. Finally, we utilize SAM [15] for assisted annotation, focusing on accurately delineating salient objects within the guided regions in the infrared image. This process results in 2,315 pairs of annotated training samples.

Representative samples from the IVOE dataset are shown in Fig. 4. The synthesized training samples demonstrate the natural distribution of light spots and precise annotations, and the test set includes diverse scenes to effectively assess the ability of model to perceive overexposure under varying conditions. Fine details, including motorcycles and other objects within overexposed regions, are meticulously annotated. This careful annotation ensures that fine details in high-exposure areas are accurately captured. Furthermore, the test set comprises only naturally overexposed real-world images, thereby establishing a reliable benchmark for assessing fusion models under extreme illumination.

E. Loss Function

EPOFusion is designed to enhance perceptual capability in overexposed scenes by preserving crucial structural and intensity details. To achieve this, we propose a composite loss function consisting of an adaptive fusion loss, a guidance segmentation loss, and a diffusion loss:

$$Loss = \zeta \mathcal{L}_{fusion} + \phi \mathcal{L}_{guidance} + \mathcal{L}_{diff}, \quad (8)$$

where ζ and ϕ are hyperparameters balancing the contributions of the fusion and guidance losses.

The image is partitioned into overexposed regions M_{oe} and normal regions M_{normal} based on the segmentation mask M . For normal regions, an intensity loss \mathcal{L}_{in} is employed to preserve the optimal intensity distribution between the visible and infrared modalities:

$$\mathcal{L}_{in}^{normal} = \|M_{normal} \odot (I_f - \max(I_{vi}, I_{ir}))\|_1 \quad (9)$$

where \odot denotes element-wise product, $\|\cdot\|_1$ denotes the ℓ_1 norm. For overexposed regions, where visible information is often unreliable, the intensity loss encourages the fused image to follow a pseudo target generated from infrared guidance:

$$\mathcal{L}_{in}^{mask} = \|M_{oe} \odot (I_f - I_{pseudo})\|_1. \quad (10)$$

To preserve structural details, a texture loss \mathcal{L}_{grad} is also applied. In normal regions, it ensures that the fused image retains prominent texture features from both modalities:

$$\mathcal{L}_{grad}^{normal} = \|M_{normal} \odot (\Delta I_f - \max(\Delta I_{vi}, \Delta I_{ir}))\|_1. \quad (11)$$

In overexposed regions, the gradient loss emphasizes infrared features, which can be amplified by a weighting factor γ :

$$\mathcal{L}_{grad}^{mask} = \|M_{oe} \odot (\Delta I_f - \gamma \Delta I_{ir})\|_1. \quad (12)$$

The total fusion loss is given by:

$$\mathcal{L}_{fusion} = \delta \mathcal{L}_{in}^{normal+mask} + \mathcal{L}_{grad}^{normal+mask}, \quad (13)$$

where $\mathcal{L}^{normal+mask}$ computes loss over normal and overexposed regions. δ is weights.

The guidance network utilizes the cross-entropy loss function, defined as follows:

$$\mathcal{L}_{seg} = - \sum_{i=1}^n q(x_i) \log(p(x_i)). \quad (14)$$

TABLE I: Quantitative comparisons of the five metrics on 361 image pairs from the MSRS dataset. The red and blue marks indicate the best and second-best values, respectively.

Category	EN \uparrow	MI \uparrow	VIF \uparrow	$Q^{AB/F}\uparrow$	SSIM \uparrow
GANMcC ₂₁ [17]	5.913	2.459	0.612	0.326	0.309
U2Fusion ₂₀ [31]	5.213	1.988	0.516	0.386	0.381
SDNet ₂₁ [5]	5.245	1.708	0.499	0.377	0.364
TarDal ₂₂ [8]	5.322	2.194	0.406	0.172	0.238
SegMif ₂₂ [4]	6.109	2.472	0.774	0.565	0.339
DDFM ₂₃ [19]	5.685	2.467	0.684	0.484	0.327
Dif-Fusion ₂₃ [18]	6.66	3.326	0.827	0.583	0.448
DCINN ₂₃ [32]	6.145	3.328	0.81	0.568	0.369
EMMA ₂₄ [33]	6.718	4.241	0.973	0.642	0.479
MRFS ₂₄ [34]	6.668	3.068	0.74	0.484	0.35
A2RNet ₂₅ [35]	6.582	3.334	0.711	0.438	0.359
TDFusion ₂₅ [25]	6.734	3.663	0.991	0.659	0.507
MaeFuse ₂₅ [36]	6.576	2.199	0.747	0.502	0.439
Ours	6.671	4.579	1.064	0.700	0.487

TABLE II: Quantitative comparisons of the five metrics on 280 image pairs from the FMB dataset;

Category	EN \uparrow	MI \uparrow	VIF \uparrow	$Q^{AB/F}\uparrow$	SSIM \uparrow
GANMcC ₂₁ [17]	6.997	3.087	0.625	0.495	0.436
U2Fusion ₂₀ [31]	6.967	3.078	0.722	0.599	0.479
SDNet ₂₁ [5]	6.807	3.177	0.623	0.557	0.456
TarDal ₂₂ [8]	6.622	3.603	0.559	0.285	0.411
SegMif ₂₂ [4]	7.018	3.201	0.812	0.675	0.452
DDFM ₂₃ [19]	6.893	3.157	0.666	0.561	0.406
Dif-Fusion ₂₃ [18]	6.663	3.215	0.585	0.526	0.362
DCINN ₂₃ [32]	6.470	3.647	0.758	0.588	0.481
EMMA ₂₄ [33]	6.772	4.032	0.833	0.648	0.455
MRFS ₂₄ [34]	6.717	3.267	0.635	0.517	0.380
A2RNet ₂₅ [35]	6.529	3.580	0.507	0.365	0.313
TDFusion ₂₅ [25]	6.987	3.427	0.836	0.660	0.510
MaeFuse ₂₅ [36]	6.939	2.535	0.597	0.473	0.391
Ours	6.672	4.823	0.930	0.716	0.463

TABLE III: Quantitative comparisons of the five metrics on 176 image pairs from the IVOE dataset;

Category	EN \uparrow	MI \uparrow	VIF \uparrow	$Q^{AB/F}\uparrow$	SSIM \uparrow
GANMcC ₂₁ [17]	6.654	2.904	0.579	0.310	0.400
U2Fusion ₂₀ [31]	6.375	2.500	0.600	0.491	0.440
SDNet ₂₁ [5]	6.007	2.053	0.516	0.433	0.417
TarDal ₂₂ [8]	6.425	3.027	0.471	0.284	0.299
SegMif ₂₂ [4]	7.149	2.841	0.718	0.594	0.418
DDFM ₂₃ [19]	6.819	3.091	0.676	0.442	0.431
Dif-Fusion ₂₃ [18]	7.182	3.800	0.722	0.562	0.431
DCINN ₂₃ [32]	7.152	3.920	0.785	0.575	0.430
EMMA ₂₄ [33]	7.311	4.794	0.901	0.639	0.464
MRFS ₂₄ [34]	7.352	3.519	0.691	0.498	0.392
A2RNet ₂₅ [35]	6.979	3.778	0.619	0.429	0.368
TDFusion ₂₅ [25]	7.338	4.075	0.895	0.650	0.491
MaeFuse ₂₅ [36]	7.210	2.605	0.677	0.502	0.427
Ours	7.196	5.137	0.912	0.664	0.464

The diffusion loss minimizes the discrepancy between true noise ϵ and the predicted noise $\hat{\epsilon}_t$:

$$\mathcal{L}_{diff} = \|\epsilon - \hat{\epsilon}_t\|_1. \quad (15)$$

Collectively, these loss components enable EPOFusion to effectively handle overexposed regions while preserving both structural fidelity and semantic consistency.

IV. EXPERMENTS

In this section, we first present the experimental configurations and evaluation metrics. Then we compare EPOFusion with other methods on several datasets, considering both qualitative and quantitative results. Finally, we validate the ability of our method to facilitate performance improvement in downstream tasks. To ensure a fair comparison, EPOFusion is trained solely on the IVOE dataset.

A. Experimental Setup

1) *Implementation Details*: All experiments, including comparative analyses and ablation studies, are performed on a system running Ubuntu 20.04 with the PyTorch 2.2.0 framework. The hardware setup includes an Intel(R) Core(TM) i7-13700KF processor operating at 3.4 GHz, 32GB of RAM, and an NVIDIA GeForce RTX 4090 GPU with 24GB of VRAM. For optimization, the AdamW optimizer [37] is used, with a linear learning rate schedule and a warm-up phase. The maximum learning rate is set to 1×10^{-5} , the batch size is 8, and the training proceeds for 1×10^5 iterations.

2) *Evaluation Metrics*: To comprehensively evaluate fusion performance, we employ a diverse set of metrics, including objective measures such as entropy (EN) and mutual information (MI) calculated in the fused image, sources-fusion-based metrics such as $Q^{AB/F}$ and structural similarity (SSIM) and the fidelity of visual information perceptual metric (VIF). For all of these metrics, higher values indicate better performance.

B. Fusion Comparison and Analysis

To evaluate the fusion performance of EPOFusion, we conduct experiments on two public RGBT datasets, namely MSRS [27] and FMB [4], as well as our IVOE dataset.

1) *Quantitative Comparison and Analysis*: We compare EPOFusion with several state-of-the-art fusion algorithms from recent years, and the quantitative results are presented in Table I, Table II, and Table III. In the MSRS dataset, EPOFusion demonstrates exceptional performance, achieving three first-place rankings and one second-place ranking, while securing the highest scores in all three key metrics. It achieves an MI of 4.579, a VIF of 1.064, and a $Q^{AB/F}$ of 0.700. These results reflect the strong ability of EPOFusion to preserve both structural and perceptual information in the fused images. Within the FMB dataset, our approach continues to excel, earning three top positions. It obtains the best VIF of 0.93 and $Q^{AB/F}$ of 0.716, together with a highly competitive second-best MI score of 4.823, demonstrating its robustness in various fusion tasks. Similarly, in the IVOE dataset, EPOFusion maintains leading performance, achieving three leading positions and on second position, with an MI of 5.137, a VIF of 0.912, and a $Q^{AB/F}$ of 0.664. This showcases its effectiveness in handling diverse datasets while retaining critical image details.

In summary, these results demonstrate that EPOFusion consistently delivers superior or highly competitive performance across diverse datasets, validating its robustness and effectiveness, and highlighting its ability to preserve critical structural and perceptual information in fused image.

2) *Qualitative Comparison and Analysis*: To better evaluate our method in overexposed scenes, we provide a comparison of the results of various fusion approaches in several representative scenarios, as shown in Fig. 6.

It can be clearly seen that methods based on generative priors such as GANMcC [17] and Dif-Fusion [18] can preserving global infrared cues effectively. However, this characteristic often leads to the introduction of modality-specific redundancy in certain scenarios, resulting in adverse visual effects. For example, in Fig. 6a, the sky region appears to be unnaturally dark compared to the visible image. This discrepancy is even more pronounced in Fig. 6d, within the high-intensity infrared license plate region, both color fidelity and brightness are significantly compromised. This limitation stems primarily from the inability of the model to differentiate between salient information and irrelevant interference, leading to the indiscriminate preservation of features from all modalities.

Fusion methods driven by downstream vision tasks effectively capture infrared details, they are often accompanied by substantial noise. For example, the outputs of SegMif [4] and TarDal [8] in Fig. 6a demonstrate that the sky region appears unusually dim and is degraded by noticeable noise artifacts. In Fig. 6c, although the structural integrity of the vehicle in the highlight region is retained, the fine texture details remain relatively blurred. A similar observation applies to Fig. 6d; while the license plate information is partially preserved, the overall imagery is dim and lacks clarity, resulting in suboptimal visual fidelity.

Fusion methods guided by handcrafted loss functions, it is observed that they fail to effectively retain infrared details when confronting overexposed scenarios. For instance, in Fig. 6a, the results from MRFS [34] and A2RNet [35] retain the high saturation intensity of the visible image in the sky region, thereby losing the vast majority of infrared texture details. Although DCINN captures some textural information, it sacrifices the thermal radiation intensity of the infrared modality. Similarly, in Fig. 6b, the output of DCINN [32] remains blurry, while MRFS [34] and A2RNet [35] fail to preserve valid infrared information.

Our method achieves a superior balance between preserving infrared information and maintaining visual fidelity. As shown in Fig. 6a, the rooftop textures in our fused result are clearly rendered with natural color gradients, and the sky region remains consistent with the visible image, effectively avoiding the introduction of redundant infrared artifacts. For the nighttime surveillance scenario in Fig. 6b, our method faithfully restores the contours and shapes of vehicle lights even within overexposed regions, yielding a natural and coordinated global fusion effect. In the nighttime driving scenario of Fig. 6c, compared to other methods, our approach not only effectively recovers vehicle texture details in highlight areas but also ensures image clarity and naturalness. Furthermore, as shown in Fig. 6d, even when facing license plate regions with extremely high infrared intensity, our method renders legible characters, while fine-grained textures such as the illumination details highlighted in the red box are excellently preserved.

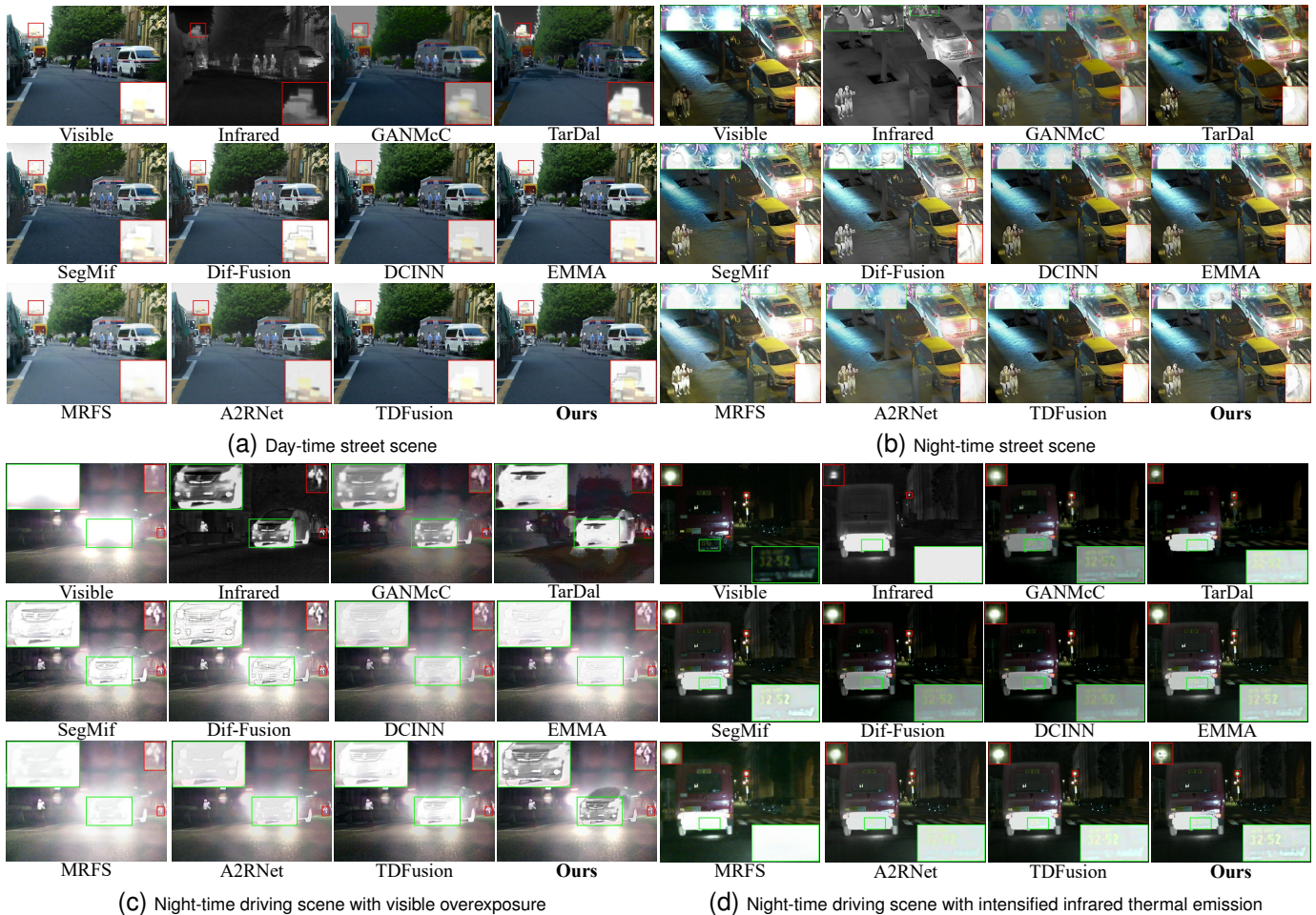


Fig. 6: Fusion results on various scenarios, comparisons are shown among visible, infrared, several SOTA methods, and our method with enlarged regions highlighting details.

TABLE IV: Ablation studies of EPOFusion. w/o denotes without. GM refers to the guidance module, AL denotes the adaptive loss.

Category	EN \uparrow	MI \uparrow	VIF \uparrow	$Q^{AB/F}\uparrow$	SSIM \uparrow
w/o GM	6.632	3.993	1.034	0.685	0.465
w/o AL	6.619	4.086	1.025	0.687	0.476
w/o DDM	6.348	2.283	0.734	0.567	0.457
w/o MSCF	6.648	3.199	0.808	0.515	0.443
EPOFusion	6.671	4.579	1.064	0.700	0.487

C. Complexity Discussion

To evaluate efficiency, we compare EPOFusion with SOTA models via FLOPs, parameters, and time. As summarized in Table V, although dual decoding branches and the iterative mechanism increase complexity, our model maintains moderate parameters (33.87M) and fast inference (74.80ms), balancing fusion quality with efficiency.

D. Performance on downstream tasks

Please refer to the Appendix for comparative results on object detection and semantic segmentation.

TABLE V: Quantitative comparison of different methods in terms of FLOPs, Params, Time on the MSRS dataset.

Method	Input Size	Params/M \downarrow	FLOPs/G \downarrow	Time/ms \downarrow
SDNet ₂₁ [5]	480x640	0.07	64.55	122.33
DDFM ₂₂ [19]	480x640	552.81	1.34M	102760
Dif-Fusion ₂₃ [18]	480x640	416.47	1056.86	809.41
SegMiF ₂₃ [4]	480x640	45.63	359.41	309.70
MRFS ₂₄ [34]	480x640	134.96	139.13	124.72
A2RNet ₂₅ [35]	480x640	3.57	164.82	239.58
MaeFuse ₂₅ [36]	480x640	325.02	1004.55	166.20
EPOFusion	480x640	33.87	149.99	74.80

E. Abalation Study

1) *Guided Fusion Framework Ablation*: In the proposed method, the guided module is designed to help the encoder focus on the most informative regions, particularly the overexposed areas where infrared information is crucial for preserving structural and semantic details. To evaluate its effectiveness, we remove the guided module and perform fusion directly using the baseline encoder-decoder structure. The quantitative results are presented in the first row of Table IV. As shown, removing the guided module leads to a performance drop in all metrics. Specifically, MI decreases from 4.579 to 3.993, SSIM decreases from 0.487 to 0.465, and $Q^{AB/F}$ declines from 0.700 to 0.685. These results

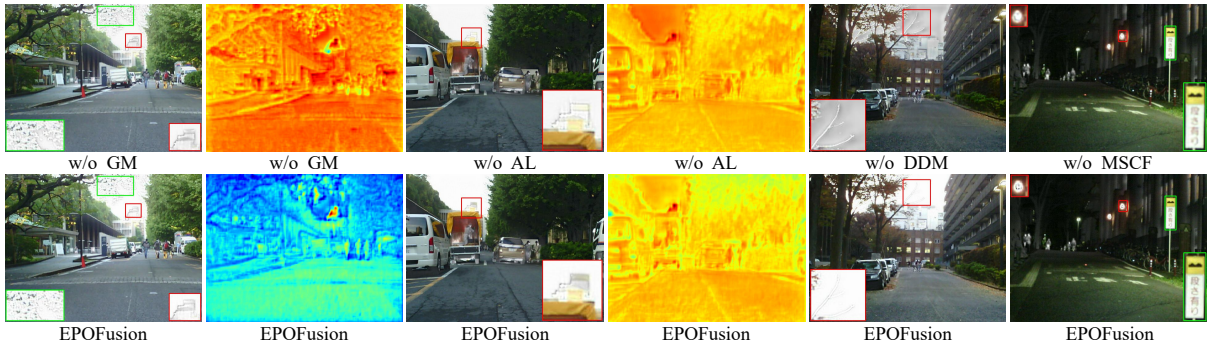


Fig. 7: Visual results and corresponding heatmaps of the ablation study on EPOFusion. w/o denotes without.

demonstrate that the guided module improves the ability of the model to preserve details from the source images.

The corresponding visual results and heatmaps are presented in the first and second columns of Fig. 7, further confirming the effectiveness of the proposed design. It can be clearly observed that with the guidance of the guided module, the model is able to accurately focus on the details within the overexposed regions while precisely highlighting the relevant areas without introducing superfluous noise.

2) *Adaptive Loss Ablation*: To evaluate the effectiveness of our proposed adaptive loss (AL), we replace it with the conventional intensity and texture losses. The quantitative results are shown in the second row of Table IV. As can be observed, compared to the guidance module (GM), the contribution of AL is more significant, since the removal of AL leads to a slight decrease across all metrics. To further demonstrate the importance of AL, we present the qualitative results in the third column of Fig. 7. When using the standard fusion loss instead, the model is able to capture infrared information in the overexposed sky regions; however, it preserves only the texture while neglecting the color intensity information. Moreover, as illustrated in the heatmap (fourth column of Fig. 7), the adaptive loss effectively guides the model to focus more precisely on the details within the overexposed areas.

3) *Iterative Decoding Fusion Module Ablation*: To evaluate the effectiveness of our proposed iterative decoding fusion module, we conduct a comprehensive ablation study on the DDM and MSCF components and analyze the influence of the number of iteration steps.

DDM Analysis: When the denoising diffusion mechanism (DDM) is removed from the decoder, performance decreases significantly in almost all metrics, as shown in the third row of Table IV. Specifically, EN decreases to 6.348, the lowest among all variants, indicating a reduced information richness in the fused images. MI also declines sharply to 2.283, showing that much less mutual information is preserved between the source and fused images. Similarly, VIF and $Q^{AB/F}$ drop to 0.734 and 0.567, respectively. The fusion result is presented in the fifth column of Fig. 7. Without DDM, the model often fails to preserve sufficient detail, and the fused result appears blurred and much less informative.

MSCF Analysis: When the MSCF module is removed, the performance decreases noticeably in multiple metrics, as shown in the fourth row of Table IV. The EN value drops to 6.648, slightly lower than the full model, indicating a reduction

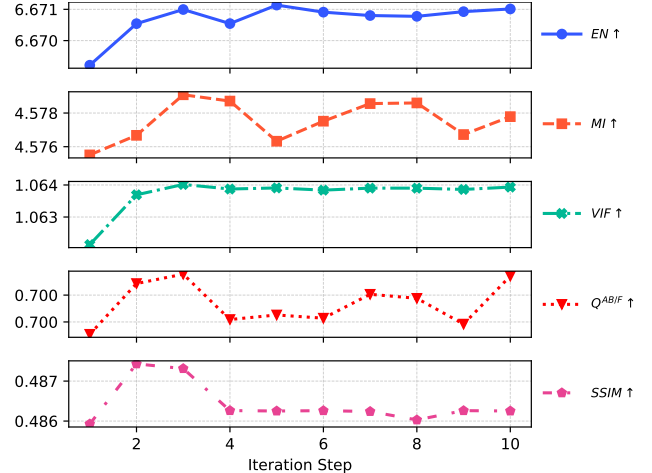


Fig. 8: Fusion performance of EPOFusion under different iteration steps.

in information diversity. MI decreases substantially to 3.199, suggesting a weaker preservation of mutual information. Similarly, VIF and $Q^{AB/F}$ drop to 0.808 and 0.515, respectively, reflecting a marked degradation in visual information fidelity and overall fusion quality. In addition, SSIM decreases to 0.443, the lowest among all ablation settings, highlighting a significant loss of structural similarity. The qualitative results in the last column of Fig. 7 further support this finding: with MSCF, the model is able to better preserve fine-grained texture details, leading to clearer fusion results. For instance, the text in the green box appears sharper and more legible, while the light textures in the red box are more distinct and clearly preserved, demonstrating the crucial role of MSCF in enhancing structural clarity and detail retention.

Iteration Step Analysis: We also present the dynamic trade-off between fusion performance and the number of steps in EPOFusion, as shown in Fig. 8. The results indicate that EPOFusion achieves optimal overall fusion with three sampling steps, effectively balancing performance and computational efficiency. As the number of steps increases, most metrics initially improve: MI, VIF, and $Q^{AB/F}$ reach their peak at step 3; EN achieves its maximum at step 4; and SSIM peaks at step 2. Beyond these points, the metrics exhibit slight declines, with a minor resurgence observed around step 8. However, increasing the number of steps also leads to a higher computational cost. To strike a balance between fusion quality and efficiency, we adopt three sampling steps for inference.

V. CONCLUSION

In this paper, we address the critical yet often overlooked challenge of overexposure in infrared and visible image fusion. To tackle this issue, we develop EPOFusion, an exposure-aware fusion model. We show that progressive optimization, implemented via iterative decoding, ensures superior feature refinement in complex scenarios. Specifically, our results confirm that explicitly guiding the encoder to recover infrared details in saturated regions is key to handling overexposed scenes effectively. Furthermore, the IVOE dataset provides essential supervision for exposure-aware learning and establishes a standard benchmark for realistic overexposed scenarios. Experiments demonstrate that EPOFusion excels at producing fused images with high visual fidelity while achieving robust performance on downstream tasks. These results validate the effectiveness and practical applicability of our approach.

ACKNOWLEDGMENTS

This work was supported partly by the National Natural Science Foundation of China under Grant No. U24A20270 and U24A20242, and National Key R&D Program of China under Grant No.2024YFC3306901.

REFERENCES

- [1] Q. Liu, Z. He, X. Li, and Y. Zheng, "Ptb-tir: A thermal infrared pedestrian tracking benchmark," *IEEE Transactions on Multimedia*, vol. 22, pp. 666–675, 2018.
- [2] X. Jia, C. Zhu, M. Li *et al.*, "Llvip: A visible-infrared paired dataset for low-light vision," *2021 IEEE/CVF International Conference on Computer Vision Workshops (ICCVW)*, pp. 3489–3497, 2021.
- [3] H. Xu, J. Ma, Z. Le, J. Jiang, and X. Guo, "Fusiondn: A unified densely connected network for image fusion," in *AAAI Conference on Artificial Intelligence*, 2020.
- [4] J. Liu, Z. Liu, G. Wu, L. Ma, R. Liu, W. Zhong, Z. Luo, and X.-Y. Fan, "Multi-interactive feature learning and a full-time multi-modality benchmark for image fusion and segmentation," *2023 IEEE/CVF International Conference on Computer Vision (ICCV)*, pp. 8081–8090, 2023.
- [5] H. Zhang and J. Ma, "Sdnet: A versatile squeeze-and-decomposition network for real-time image fusion," *International Journal of Computer Vision*, vol. 129, pp. 2761 – 2785, 2021.
- [6] J. Ma, W. Yu, P. Liang, C. Li, and J. Jiang, "Fusiongan: A generative adversarial network for infrared and visible image fusion," *Inf. Fusion*, vol. 48, pp. 11–26, 2019.
- [7] J. Li, H. Huo, C. Li *et al.*, "Attentionfgan: Infrared and visible image fusion using attention-based generative adversarial networks," *IEEE Transactions on Multimedia*, vol. 23, pp. 1383–1396, 2021.
- [8] J. Liu, X. Fan, Z. Huang, G. Wu, R. Liu, W. Zhong, and Z. Luo, "Target-aware dual adversarial learning and a multi-scenario multi-modality benchmark to fuse infrared and visible for object detection," *2022 IEEE/CVF Conference on Computer Vision and Pattern Recognition (CVPR)*, pp. 5792–5801, 2022.
- [9] A. Dong, L. Wang, J. Liu *et al.*, "Co-enhancement of multi-modality image fusion and object detection via feature adaptation," *IEEE Transactions on Circuits and Systems for Video Technology*, vol. 34, pp. 12 624–12 637, 2024.
- [10] I. J. Goodfellow, J. Pouget-Abadie, M. Mirza, B. Xu, D. Warde-Farley, S. Ozair, A. Courville, and Y. Bengio, "Generative adversarial nets," *Advances in neural information processing systems*, vol. 27, 2014.
- [11] X. Zhang, L. Wang, L. Zhao, X. Li, and S. Ma, "A semantic-aware and multi-guided network for infrared-visible image fusion," *IEEE Transactions on Multimedia*, pp. 1–13, 2025.
- [12] Y. Zhao, Q. Zheng, P. H. Zhu, X. Zhang, and W. Ma, "Tufusion: A transformer-based universal fusion algorithm for multimodal images," *IEEE Transactions on Circuits and Systems for Video Technology*, vol. 34, pp. 1712–1725, 2024.
- [13] L. Tang, Z. Chen, J. Huang, and J. Ma, "Camf: An interpretable infrared and visible image fusion network based on class activation mapping," *IEEE Transactions on Multimedia*, vol. 26, pp. 4776–4791, 2024.
- [14] J. Ho, A. Jain, and P. Abbeel, "Denoising diffusion probabilistic models," *Advances in neural information processing systems*, vol. 33, pp. 6840–6851, 2020.
- [15] A. Kirillov, E. Mintun, N. Ravi, H. Mao, C. Rolland, L. Gustafson, T. Xiao, S. Whitehead, A. C. Berg, W.-Y. Lo, P. Dollár, and R. B. Girshick, "Segment anything," *2023 IEEE/CVF International Conference on Computer Vision (ICCV)*, pp. 3992–4003, 2023.
- [16] J. Ma, P. Liang, W. Yu, C. Chen, X. Guo, J. Wu, and J. Jiang, "Infrared and visible image fusion via detail preserving adversarial learning," *Inf. Fusion*, vol. 54, pp. 85–98, 2020.
- [17] J. Ma, H. Zhang, Z. Shao, P. Liang, and H. Xu, "Ganmcc: A generative adversarial network with multiclassification constraints for infrared and visible image fusion," *IEEE Transactions on Instrumentation and Measurement*, vol. 70, pp. 1–14, 2021.
- [18] J. Yue, L. Fang, S. Xia, Y. Deng, and J. Ma, "Dif-fusion: Toward high color fidelity in infrared and visible image fusion with diffusion models," *IEEE Transactions on Image Processing*, vol. 32, pp. 5705–5720, 2023.
- [19] Z. Zhao, H. Bai, Y. Zhu, J. Zhang, S. Xu, Y. Zhang, K. Zhang, D. Meng, R. Timofte, and L. V. Gool, "Ddfm: Denoising diffusion model for multi-modality image fusion," *2023 IEEE/CVF International Conference on Computer Vision (ICCV)*, pp. 8048–8059, 2023.
- [20] J. Li, C. Jiang, J. Jiang *et al.*, "Towards unified semantic and controllable image fusion: A diffusion transformer approach," *IEEE Transactions on Pattern Analysis and Machine Intelligence*, 2025.
- [21] K. Zhang, L. Sun, J. Yan *et al.*, "Texture-content dual guided network for visible and infrared image fusion," *IEEE Transactions on Multimedia*, vol. 27, pp. 2097–2111, 2025.
- [22] Q. Yang, K. Ren, and Q. Chen, "Amsfusion: An adaptive multi-scale infrared and visible image fusion network based on attention mechanisms," *IEEE Transactions on Circuits and Systems for Video Technology*, 2025.
- [23] R. Xie, M. Tao, H. Xu, M. Chen, D. Yuan, and Q. Liu, "Overexposed infrared and visible image fusion benchmark and baseline," *Expert Syst. Appl.*, vol. 266, p. 126024, 2024.
- [24] Z. Wang, D. He, L. Zhao, B. Liu, Y. Zheng, and X. Zhang, "Difusionseg: Diffusion-driven semantic segmentation with multi-modal image fusion for enhanced perception," *Knowledge-Based Systems*, 2025.
- [25] H. Bai, J. Zhang, Z. Zhao *et al.*, "Task-driven image fusion with learnable fusion loss," *2025 IEEE/CVF Conference on Computer Vision and Pattern Recognition (CVPR)*, pp. 7457–7468, 2024.
- [26] Q. Ha, K. Watanabe, T. Karasawa, Y. Ushiku, and T. Harada, "Mfnnet: Towards real-time semantic segmentation for autonomous vehicles with multi-spectral scenes," *2017 IEEE/RSJ International Conference on Intelligent Robots and Systems (IROS)*, pp. 5108–5115, 2017.
- [27] L. Tang, J. Yuan, and J. Ma, "Image fusion in the loop of high-level vision tasks: A semantic-aware real-time infrared and visible image fusion network," *Inf. Fusion*, vol. 82, pp. 28–42, 2022.
- [28] Z. Liu, H. Mao, C. Wu, C. Feichtenhofer, T. Darrell, and S. Xie, "A convnet for the 2020s," *2022 IEEE/CVF Conference on Computer Vision and Pattern Recognition (CVPR)*, pp. 11 966–11 976, 2022.
- [29] J. Song, C. Meng, and S. Ermon, "Denoising diffusion implicit models," *ArXiv*, vol. abs/2010.02502, 2020.
- [30] X. Zhang, P. Ye, and G. Xiao, "Vifb: A visible and infrared image fusion benchmark," *2020 IEEE/CVF Conference on Computer Vision and Pattern Recognition Workshops (CVPRW)*, pp. 468–478, 2020.
- [31] H. Xu, J. Ma, J. Jiang, X. Guo, and H. Ling, "U2fusion: A unified unsupervised image fusion network," *IEEE Transactions on Pattern Analysis and Machine Intelligence*, vol. 44, pp. 502–518, 2020.
- [32] W. Wang, L. Jian Deng, R. Ran, and G. Vivone, "A general paradigm with detail-preserving conditional invertible network for image fusion," *Int. J. Comput. Vis.*, vol. 132, pp. 1029–1054, 2023.
- [33] J.-J. Hwang, R. Xu, H. Lin *et al.*, "Emma: End-to-end multimodal model for autonomous driving," *Trans. Mach. Learn. Res.*, vol. 2025, 2024.
- [34] H. Zhang, X. Zuo, J. Jiang *et al.*, "Mrfs: Mutually reinforcing image fusion and segmentation," *2024 IEEE/CVF Conference on Computer Vision and Pattern Recognition (CVPR)*, pp. 26 964–26 973, 2024.
- [35] J. Li, H. Yu, J. Chen *et al.*, "A2rnet: Adversarial attack resilient network for robust infrared and visible image fusion," in *AAAI Conference on Artificial Intelligence*, 2024.
- [36] J. Li, J. Jiang, P. Liang, J. Ma, and L. Nie, "Maefuse: Transferring omni features with pretrained masked autoencoders for infrared and visible image fusion via guided training," *IEEE Transactions on Image Processing*, vol. 34, pp. 1340–1353, 2025.
- [37] I. Loshchilov and F. Hutter, "Decoupled weight decay regularization," in *International Conference on Learning Representations*, 2017.

- [38] E. Xie, W. Wang, Z. Yu, A. Anandkumar, J. M. Álvarez, and P. Luo, "Segformer: Simple and efficient design for semantic segmentation with transformers," in *Neural Information Processing Systems*, 2021.
- [39] R. Khanam and M. Hussain, "Yolov11: An overview of the key architectural enhancements," *ArXiv*, vol. abs/2410.17725, 2024.

VI. SUPPLEMENTARY MATERIAL

A. Downstream tasks Comparison

To assess the performance of our method in handling overexposed scenarios for downstream vision tasks, we conduct experiments on two public datasets: MSRS [27] for semantic segmentation and M³FD [8] for object detection. Given the scarcity of overexposed scenes in existing datasets, we adopt the data construction strategy described in Section III.D, where Gaussian spots are superimposed on target objects to simulate overexposure. We employ SegFormer [38] for segmentation and YOLOv11 [39] for object detection. In all experiments, we first apply each fusion method to both the training and test sets, and subsequently train the detection and segmentation models for the same number of iterations under identical settings.

1) *Segmentation Comparison and Analysis:* As presented in Table VI, our method demonstrates superior performance in semantic segmentation across nine categories. It achieves a top-ranking mean Intersection over Union (mIoU) score of 73.89%, a significant 2.1% improvement over the second-best method, SegMif [4], which scored 71.789%. A detailed analysis reveals our method ranks first in six of the nine categories, particularly excelling in challenging ones that demand fine detail preservation. For instance, it achieves leading IoU scores of 78.86% for guardrail, 74.16% for bump, 73.07% for car stop, and 53.91% for curve, outperforming the runner-up methods in the first three categories by 2.85%, 3.92%, and 2.12%, respectively. While maintaining competitive performance on prominent objects like Car with a score of 87.65%, this strong performance on complex categories underscores unique capability of our model to preserve details in overexposed regions, instead of merely emphasizing salient objects.

The visual results are presented in Fig. 9. To better evaluate our method we also present the fusion result in Fig. 10. For the first daytime scene, as shown in Fig. 10, severe overexposure significantly degrades the visible image features. In contrast to competing methods, our method effectively reveals the pedestrian within the overexposed region while preserving fine-grained details. Consequently, EPOFusion accurately delineates the pedestrian, generating complete and precise segmentation masks that are highly consistent with the Ground Truth. The second row displays a challenging nighttime scenario characterized by low ambient light and strong glare from a light source. As observed in the comparison, this overexposure leads to significant feature loss, particularly for the pedestrian near the light source. Consequently, many competing methods fail to generate coherent masks, resulting in fragmented segmentation for the pedestrian (green box) and inaccurate, blurred boundaries for the bottom of the car (red box). In contrast, EPOFusion achieves superior segmentation of fine details. As evidenced by the fusion results in Fig. 9, our method preserves richer texture in the wheel region of car and maximally retains the contour information of the distant pedestrian.

2) *Detection Comparison and Analysis:* The detection results presented in Table VII demonstrate the clear superiority of our method over existing approaches. Our model achieves the highest mAP@50 score of 0.851, surpassing the second-best method, U2Fusion [31], by a margin of 1.8%. A detailed per-category analysis confirms this strong performance, showing that our method ranks first in six out of the seven metrics. It secures top AP@50 scores with values of 0.865 for people, 0.923 for car, 0.724 for motorcycle, 0.801 for lamp, and 0.889 for truck. This consistent, leading performance across diverse object classes demonstrates that EPOFusion is optimized for robust downstream detection, particularly in challenging overexposed scenes.

The fusion and object detection results are presented in Fig. 11. In the daytime scenario, our proposed method maintains superior visual fidelity compared to competing algorithms. Our method effectively mitigates these high-highlight artifacts by integrating complementary thermal intensity, thereby clearly revealing targets within the overexposed regions. This visual enhancement directly benefits downstream tasks. Specifically, our method successfully detects the small lamp on the right side of the image, a subtle object that is frequently missed by other fusion methods due to low contrast or background clutter. In the nighttime scene, EPOFusion effectively mitigates the impact of strong light interference, successfully revealing and detecting the car located within the heavily overexposed region, which is a target often obscured in visible images. Moreover, the spatial structure and position of the signal light are distinctly preserved, ensuring accurate localization. These results indicate that our method preserves crucial infrared details under challenging exposure conditions, which is essential for reliable object detection.

Overall, the results of EPOFusion are particularly suitable for downstream tasks, especially in overexposed scenarios, highlighting its robustness and practical applicability.

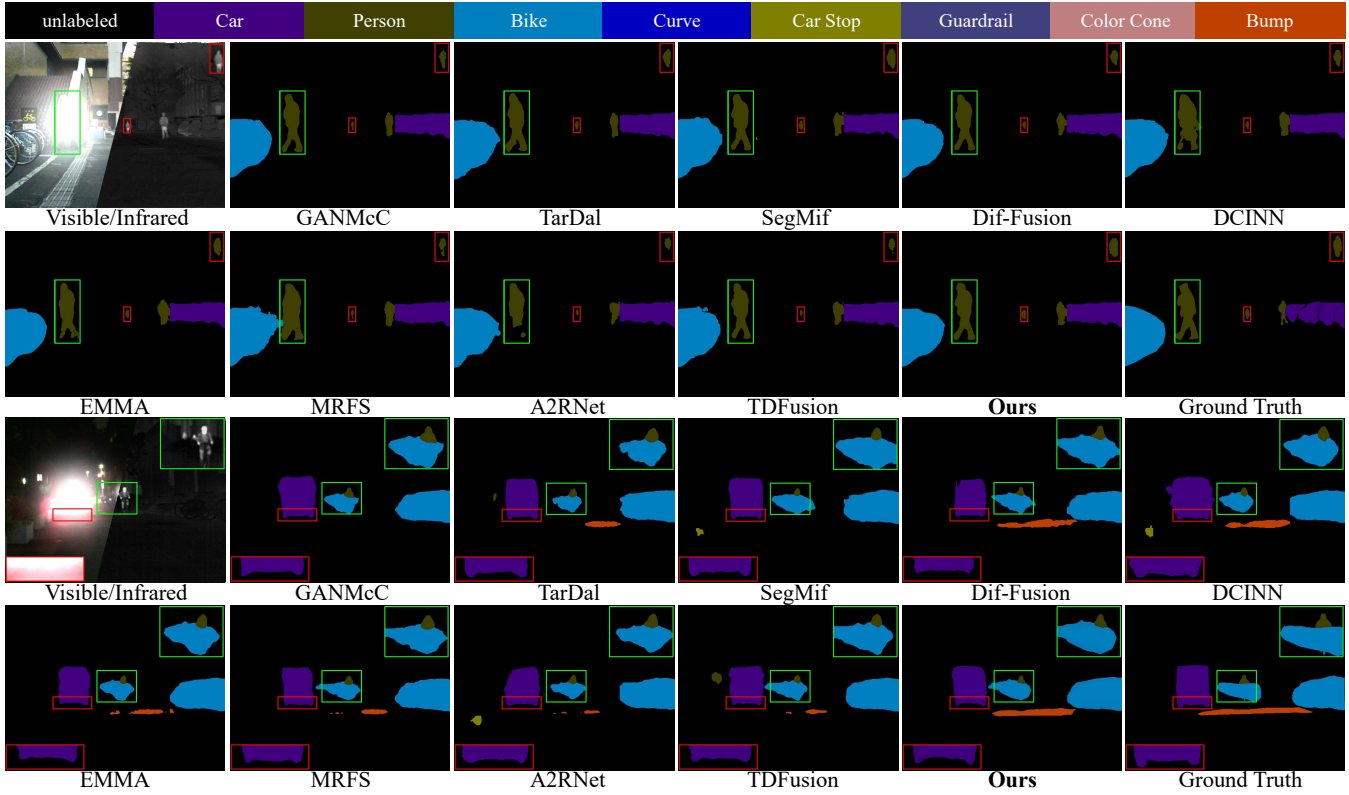


Fig. 9: Segmentation results for scenes 00404D and 01004N with various fusion algorithms on the MSRS dataset with simulated glare. Each pair of rows represent a scene, arranged from top to bottom.



Fig. 10: Fusion results for scenes 00404D and 01004N with various fusion algorithms on the MSRS dataset with simulated glare.

TABLE VI: Comparison of mIoU across different categories and methods.

Category	IoU%												Ours
	GANMcC	U2Fusion	SDNet	TarDal	SegMif	Dif-Fusion	DDFM	DCINN	EMMA	MRFS	A2RNet	TDFusion	
Background	98.04	98.18	98.16	97.8	98.09	97.99	97.79	97.91	97.91	97.85	97.89	98.07	98.21
Car	85.7	87.84	87.39	84.32	86.73	85.26	84.7	85.31	85.19	83.91	84.53	86.81	87.65
Person	70.41	70.98	72.17	66.6	69.68	68.46	66.91	65.81	65.06	64.18	63.63	68.35	68.53
Bike	69.12	70.45	69.6	67.97	70.47	68.48	66.64	68.33	68.4	68.46	68.86	70.64	70.01
Curve	50.88	47.02	49.62	40.22	51.39	51.28	39.57	46.92	47.38	48.32	46.09	46.5	53.91
Car Stop	68.92	70.81	69.41	68.04	71.21	71.87	63.83	71.15	67.61	67.84	68.77	70.95	73.07
Guardrail	68.98	69.86	71.67	62.7	68.94	75.13	59.78	72.05	59.02	67.15	76.01	68.61	78.86
Color Cone	59.13	59.94	60.24	55.15	59.47	59	51	58.11	53.6	57.57	55.16	59.38	60.59
Bump	70.66	68.96	67.51	64.67	70.12	65.19	62.71	68.52	70.63	70.58	67.41	68.04	74.16
mIoU	71.316	71.56	71.752	67.497	71.789	71.407	65.881	70.457	68.311	69.599	69.833	70.817	73.888

TABLE VII: Comparison of AP@50 across different categories and methods.

Category	AP@50												Ours
	GANMcC	U2Fusion	SDNet	TarDal	SegMif	Dif-Fusion	DDFM	DCINN	EMMA	MRFS	A2RNet	TDFusion	
People	0.843	0.843	0.836	0.802	0.836	0.834	0.839	0.826	0.817	0.807	0.823	0.819	0.865
Car	0.914	0.914	0.915	0.903	0.916	0.908	0.906	0.909	0.909	0.898	0.893	0.91	0.923
Bus	0.887	0.896	0.925	0.859	0.908	0.895	0.889	0.888	0.893	0.838	0.843	0.884	0.903
Motorcycle	0.672	0.709	0.681	0.649	0.648	0.68	0.684	0.623	0.614	0.597	0.577	0.623	0.724
Lamp	0.786	0.783	0.758	0.749	0.769	0.779	0.757	0.781	0.752	0.734	0.737	0.752	0.801
Truck	0.868	0.850	0.866	0.819	0.862	0.843	0.829	0.825	0.824	0.81	0.825	0.844	0.889
mAP@50	0.828	0.833	0.83	0.797	0.823	0.823	0.817	0.809	0.802	0.781	0.783	0.805	0.851

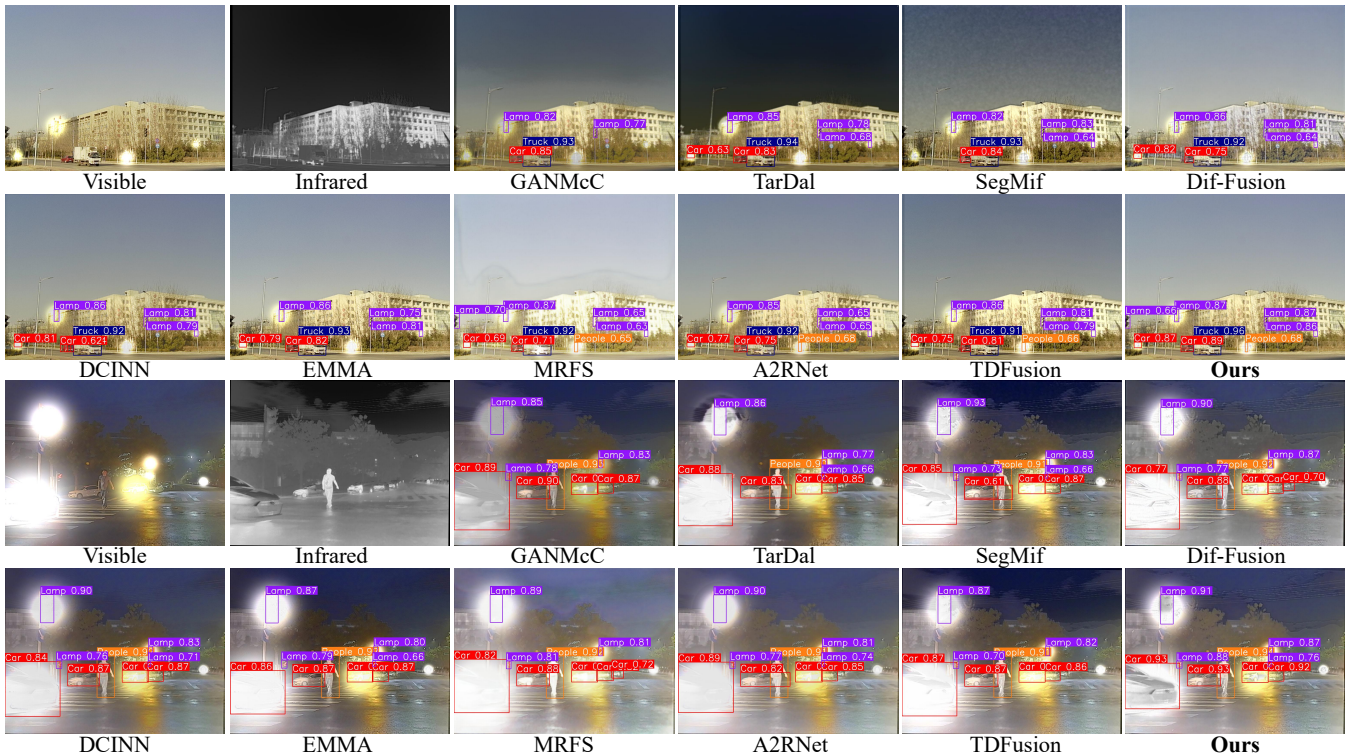


Fig. 11: Fusion and object detection results for scenes 02619 and 00465 with various fusion algorithms on the M³FD dataset with simulated glare.